actuators

MDPI

Article

Torque Differential-Based Dynamic Modeling, Validation, and Steering Characteristics Analysis of Multi-Axial Skid-Steered Wheeled Vehicle

Yuzheng Zhu, Shihua Yuan, Xueyuan Li *, Ao Li and Xin Gao

The School of Mechanical Engineering, Beijing Institute of Technology, Beijing 100081, China; 3120205197@bit.edu.cn (Y.Z.); yuanshihua@bit.edu.cn (S.Y.); 3120230295@bit.edu.cn (A.L.); x.gao@bit.edu.cn (X.G.)
* Correspondence: lixueyuan@bit.edu.cn

Abstract: Skid-steered technology has been widely applied to wheeled vehicles due to its advanced pivot steering capabilities and adaptable power transmission systems. To better understand the steering characteristics of skid-steered wheeled vehicles and derive general conclusions, a torque differential-based (TD-based) two-degree-of-freedom (2-DOF) dynamic model was developed. This model is grounded in the vehicle's steering mechanism and the single-wheel dynamics model, and a steering radius model based on TD input was established using the concept of the instantaneous center of rotation (ICR). Additionally, an expression for the stability factor was derived, and both the steady-state and transient steering characteristics were analyzed. Finally, the real vehicle tests demonstrated that the TD-based dynamic model responds quickly, maintains high precision, and remains stable across different steering input frequencies. Compared with the SD-based dynamic model, the TD-based dynamic model has a 2.553% higher calculation accuracy for the steering radius, a 6.251% higher comprehensive response accuracy for the steering input, and a response speed advantage of 1.035%.

Keywords: skid-steered vehicle; torque differential; dynamic model; steering characteristics; experimental validation

check for updates

Academic Editor: Keigo Watanabe

Received: 5 December 2024
Revised: 30 December 2024
Accepted: 2 January 2025
Published: 4 January 2025

Citation: Zhu, Y.; Yuan, S.; Li, X.; Li, A.; Gao, X. Torque Differential-Based Dynamic Modeling, Validation, and Steering Characteristics Analysis of Multi-Axial Skid-Steered Wheeled Vehicle. *Actuators* **2025**, *14*, 13. https://doi.org/10.3390/act14010013

Copyright: © 2025 by the authors. Licensee MDPI, Basel, Switzerland. This article is an open access article distributed under the terms and conditions of the Creative Commons Attribution (CC BY) license (https://creativecommons.org/licenses/by/4.0/).

1. Introduction

Skid-steered wheeled vehicles, distinguished by advanced pivot steering capabilities and adaptable power transmission systems, are essential in applications requiring peak steering agility and optimal space utilization [1,2]. These vehicles transcend traditional Ackermann steering limitations, circumventing steering trapezoid constraints to achieve zero-radius turning, thereby substantially improving maneuverability and passability [3,4]. Steering in skid-steered wheeled vehicles is facilitated by distinct tire–road interactions on each side, characterized by differential torque and rotational speeds. The steering system in skid-steered wheeled vehicles optimizes the power transmission system layout by eliminating traditional mechanical steering components and requisite tire turning space [5].

Skid-steering revises vehicle steering mechanics, affecting performance and lateral dynamics. Compared to Ackermann systems, research on skid-steering's impact on lateral dynamics and performance remains incipient, with unclear effects on control response [6,7]. The dynamics model of this steering system lacks ideal precision, complicating the optimization design, system integration, and control strategy implementation for skid-steered wheeled vehicles [8]. Scholars are actively advancing research into the dynamics and

steering performance of skid-steered wheeled vehicles. Tire–road contact, foundational to vehicle drive and steering forces, initiates scholarly research on skid-steering characteristics. Analysis of steering forces encompasses multibody dynamics simulations, tire–road shear mechanics, and linear dynamics models to assess differential steering characteristics [9,10].

Multibody dynamics simulation integrates elastic tire models with rigid body models to develop a coupled vehicle–body–tire multiphysics model. This approach enables the analysis and evaluation of skid-steering characteristics across diverse road surface models under varied steering inputs [11,12]. Standard software like DADS (MotionPort, La Cañada Flintridge, CA, USA) [13], ADAMS (MSC Software, Newport Beach, CA, USA) [14], and AMEsim (Siemens Digital Industries Software, Plano, TX, USA) [15] constructs comprehensive vehicle models. These models apply specific steering inputs to assess responses under varied conditions. While precise for targeted research, this method's need for model reconfiguration upon changing subjects limits its ability to generalize findings on steering characteristics.

Tire–road shear mechanics use equations to model tire-road interactions, enabling integrated analysis of tire deformation and ground mechanics [16,17]. Numerical simulations establish forward dynamics equations for skid-steered wheeled vehicles, incorporating variables like tire pressure and ground conditions to evaluate steering characteristics under varied scenarios [18]. Shear stress is expressed through spatial vector algebra [19], finite element methods [20], or empirical formulas based on the Coulomb friction model [12]. This method requires extensive computational analysis of tire–road interactions to accurately simulate tire forces, particularly those variations caused by tire deformation. As in the initial method, altering the research focus significantly influences the computational framework, preventing generalizable conclusions.

In contrast, the analysis of Ackermann steering characteristics provides a general formula for describing steering behaviors. This approach involves defining steering inputs and deriving tire forces under plausible assumptions based on the tire model, enabling the formulation of a linear two-degree-of-freedom (2-DOF) dynamics model for skid-steered wheeled vehicles [21,22]. The definition of steering inputs is crucial for analyzing the steering dynamics. Generalized lateral dynamic models for 4×4 [23], 6×6 [24], and 8×8 [25] skid-steered wheeled vehicles configurations have been developed based on speed differential (SD) inputs $\Delta u / v_x$, excluding second-order steering input terms. This facilitates the development of general formulas for stability factors and the analysis of steady-state and transient steering behaviors. Ossama [26] integrated direct yaw moment requirements with a traditional 2-DOF linear model to analyze steering responses, clarifying the relationship between steering behaviors and yaw moments. The linear modeling approach provides general formulas suitable for various research subjects, enabling the analysis of steering traits akin to Ackermann vehicles; however, it is limited by its inability to account for tire non-linearities and inherent model precision constraints.

From the perspective of multi-axle skid-steered vehicle control, SD-based control methods achieve smooth steering under nominal conditions. However, a key limitation emerges when a wheel slips or becomes immobilized (e.g., in mud, sand, or snow) [27]. In these scenarios, torque is concentrated on the slipping wheel, depriving other wheels of sufficient drive torque. This causes a severe loss of propulsion in complex terrains, rendering SD-based control unsuitable for sustained off-road operations. In contrast, torque-differential-based control effectively addresses these limitations. By the limited-slip mechanisms, the wheel speed will be limited differences during slippage, and torque will be redistributed to wheels with greater traction. This ensures vehicle mobility and maneuverability while significantly improving stability, traction, and reliability in off-road conditions [28,29].

Recent investigations reveal preliminary advancements in the modeling and theoretical analysis of skid-steered wheeled vehicles, though challenges remain concerning model accuracy and generalizability. Identified issues include the following:

1. Analytical methods employing numerical and multibody dynamics simulations that do not yield a universal mechanical expression for the lateral dynamics of skid-steered vehicles, thereby limiting their theoretical applicability.
2. Approaches interpreting differential steering strictly through speed differences as steering inputs inadequately probe the fundamental steering mechanisms. Moreover, these methods frequently overlook second-order terms related to steering inputs during model construction, compromising the derived lateral dynamics model's accuracy.

To address these limitations, this study builds upon skid-steering principles using linearization assumptions for theoretical derivations. An innovative lateral dynamics model for multi-axial skid-steered vehicles based on torque differential (TD) inputs has been developed, providing extensive analysis of steering characteristics and key motion parameter responses and variations. This model has been validated through empirical testing with actual vehicles, aiming to enhance precision and broaden the applicability of theories concerning differential steering vehicles. The main contributions can be summarized as follows:

Contribution 1: Establishment of a general expression for a TD-based linear dynamics model of skid-steered wheeled vehicles, including calculations for stability factors and steady-state steering radius.

Contribution 2: Integration of the dynamics model for detailed analysis of skid-steered vehicles' steering characteristics, focusing on yaw rate, side slip angle, and steering radius responses and variations.

Contribution 3: Utilization of an electrically driven skid-steered vehicle to benchmark the proposed dynamics model against the SD-based model, demonstrating a greater response and accuracy.

The remainder of this article is arranged as follows. In the second section, the planar motion of the vehicle and the ICRs are modeled, and the SD-based linear 2-DOF dynamic model of the skid-steered vehicle is extended to the multi-axle vehicle. In the third section, a TD-based linear 2-DOF dynamic model of the skid-steered vehicle is established. According to the model, the expression of parameters such as "stability factor" is obtained and its steady-state and transient steering response characteristics are analyzed. In the fourth section, the two dynamic models are compared and verified by a real vehicle test, and the response characteristics of the two models under step and pulse input are analyzed.The framework of this paper is shown in Figure 1.

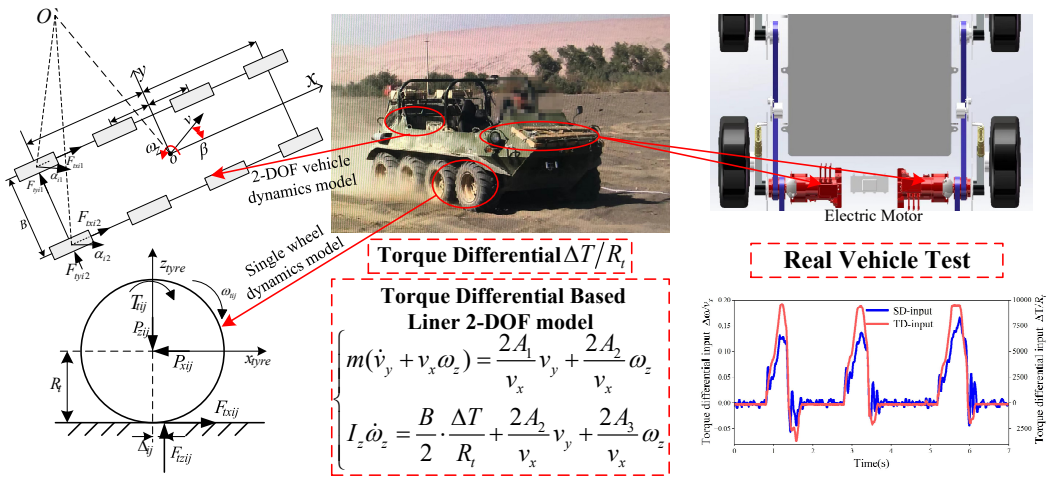


Figure 1. Architecture of our research object, method, model, and text process. The torque differential is clarified by the single wheel dynamics model and the characteristics of the skid-steering electric drive system based on the 2-DOF vehicle dynamics model, then the TD-based 2-DOF dynamic model is established to describe the steering characteristics. Additionally, the real vehicle test is carried out to prove the performance of the model.

2. System Model Establishment

In vehicle dynamics modeling, it is often impractical to fully capture all vehicle characteristics. As a result, the modeling process is typically simplified, focusing on key aspects relevant to the research objective, while neglecting factors with minimal impact on the specific study. To investigate the steering behavior of multi-axle skid-steered wheeled vehicles, a 2-DOF vehicle dynamics model, an instantaneous center of rotation (ICR) model, and a single-wheel dynamics model were developed. These models provide the foundational framework for the subsequent development of the TD-based 2-DOF model. Additionally, a comparative SD-based model was formulated, and the steering response characteristics were analyzed.

2.1. Vehicle Dynamics Model

Compared to the Ackermann steering mechanism, skid-steering achieves directional changes through the differential speed or torque of the wheels, without wheel slip, thus precluding the application of the "bicycle model" analogy for linear model development. Nevertheless, rational assumptions derived from steady-state steering principles can be perpetuated.

The following assumptions are considered in the modeling process:

1. The vehicle is approximated as a rigid body, with the suspension system effects neglected, and the vehicle's motion is confined to the horizontal xoy plane;
2. The vehicle's longitudinal velocity is assumed to be constant, with aerodynamic drag effects excluded;
3. The transverse and longitudinal accelerations are presumed to be minimal, ensuring that the tire's longitudinal slip and lateral force characteristics operate within the linear regime;
4. The steering angle of the vehicle is deemed to be small, validating the small-angle approximation, i.e., $\tan\delta = \sin\delta = \delta$, $\cos\delta = 1$.

The lateral and yaw motions that best reflect the stability issues are examined in this paper. Considering the planar motion of the skid-steered vehicle as shown in Figure 1,

one can establish the general expression for a 2-DOF dynamics model of a multi-axle skid-steered vehicle [30].

$$\begin{cases} m(\dot{v}_y + v_x\omega_z) = \sum_1^n \sum_1^2 F_{tyij} \\ I_z\dot{\omega}_z = \sum_1^n L_i(F_{tyi1} + F_{tyi2}) + \frac{B}{2}\sum_1^n (F_{txi2} - F_{txi1}) \end{cases}. \tag{1}$$

where v_x represents the longitudinal velocity; v_y represents the lateral velocity; ω_z represents the yaw rate; F_{txij} represents the longitudinal force of each tire; F_{tyij} represents the lateral force of each tire; m represents the mass of the vehicle; I_z represents the moment of inertia about the z-axis; L_i represents the distance between each axis to the center of mass; L_i is directional, and assumes a positive value when the corresponding axis is located ahead of the center of mass; B represents the width of the vehicle; i represents the axle number;and j represents whether it is the left or right side.

Combining the small-angle assumption, the side slip angle α_{ij} of each tire for the skid-steered vehicle can be expressed as

$$\alpha_{ij} = \arctan\frac{v_{tyij}}{v_{txij}} \approx \frac{v_{tyij}}{v_{txij}}, \tag{2}$$

where v_{txij} and v_{txij} represent the longitudinal and lateral speeds of the tire.

$$\begin{cases} v_{txij} = v_x \pm \frac{B}{2}\omega_z \\ v_{tyij} = v_y + L_i\omega_z \end{cases}, \tag{3}$$

where the "±" term arises from the yaw motion; it takes a negative sign when j = 1 and a positive sign when j = 2.

2.2. Single Wheel Dynamics Model

Each tire possesses two degrees of freedom: one is the vertical hopping of the wheel due to road surface irregularities, and the other is the rotational motion of the wheel [31]. The specific tire dynamics model is illustrated in Figure 1.

Under the assumptions of planar motion in this study, where the vertical hopping of the wheels is zero, the dynamics model for the rotational motion of the wheels is given by

$$I_{tij}\dot{\omega}_{tij} = T_{tij} - F_{tzij}\Delta_{ij} - F_{txij}R_t, \tag{4}$$

where I_{tij} represents the rotational inertia of the tire; ω_{tij} represents the angular velocity of the tire; R_t represents the radius of the tire; T_{tij} represents the driving or braking torque on the whole tire; and Δ_{ij} represents the offset distance caused by the vertical force acting off-center from the tire.

The offset distance is caused by the elastic deformation and rolling friction that result from the contact between the tire and the ground, which forms a resisting torque in the center of the wheel. This resisting torque can be expressed as

$$F_{tzij}\Delta_{ij} = F_{tzij} \cdot f_f R_t. \tag{5}$$

2.3. Instantaneous Center of Rotation Model

The steady-state steering radius is a critical parameter for evaluating vehicle steering performance. For Ackermann steering vehicles constrained by trapezoidal geometry, the steady-state steering radius is determined through geometric methods using steering angle inputs. In contrast, in skid-steered vehicles unconstrained by trapezoidal geometry, the steering radius cannot be calculated directly. Instead, determining the steady-state steering

radius necessitates the use of ICR coordinates, which enables the analysis of steering response characteristics across various vehicle models.

Analogous to tracked vehicles, the ground contact dynamics of skid-steered wheeled vehicles constitute a composite motion, resulting from two distinct kinematic elements. Referring to the principles of tracked vehicle operation, the ICR of skid-steered vehicles is analyzed. As shown in Figure 2, ICR_v represents the ICR position of the vehicle, ICR_1 and ICR_2 represent the ICR of the left and right wheels, respectively. The steering process of the skid-steered wheeled involves a conscripted motion $\tilde{\mathbf{V}}_\mathbf{q}$, which is the overarching rotational movement of the vehicle around ICR_v. The relative motion $\tilde{\mathbf{V}}_\mathbf{x}$ entails the rotational linear velocity at the tire contact patch. Together, these elements synergistically generate the absolute motion $\tilde{\mathbf{V}}_\mathbf{j}$, characterized by the rotation around ICR_1 and ICR_2 adjacent to the tire contact patch. The L point and R point, respectively, denote the intersection points where lines from the left and right tire contact patches meet the three ICRs.

According to reference [32], it can be proven that the longitudinal coordinates of the vehicle's ICRs are the same as those of the left and right wheels, meaning the three centers lie on the same straight line. By analyzing the velocity vectors at the L and R point, it can be deduced that the line defined by these points is parallel to the y-axis of the vehicle coordinate system, which denotes $x_{ICR_v} = x_{ICR_1} = x_{ICR_2}$.

Based on the kinematic relationships of the vehicle, the expression for the coordinates of the ICR is

$$\begin{cases} x_{ICR_v} = x_{ICR_1} = x_{ICR_2} = -\frac{v_y}{\omega_z} \\ y_{ICR_v} = \frac{v_x}{\omega_z} \end{cases}. \tag{6}$$

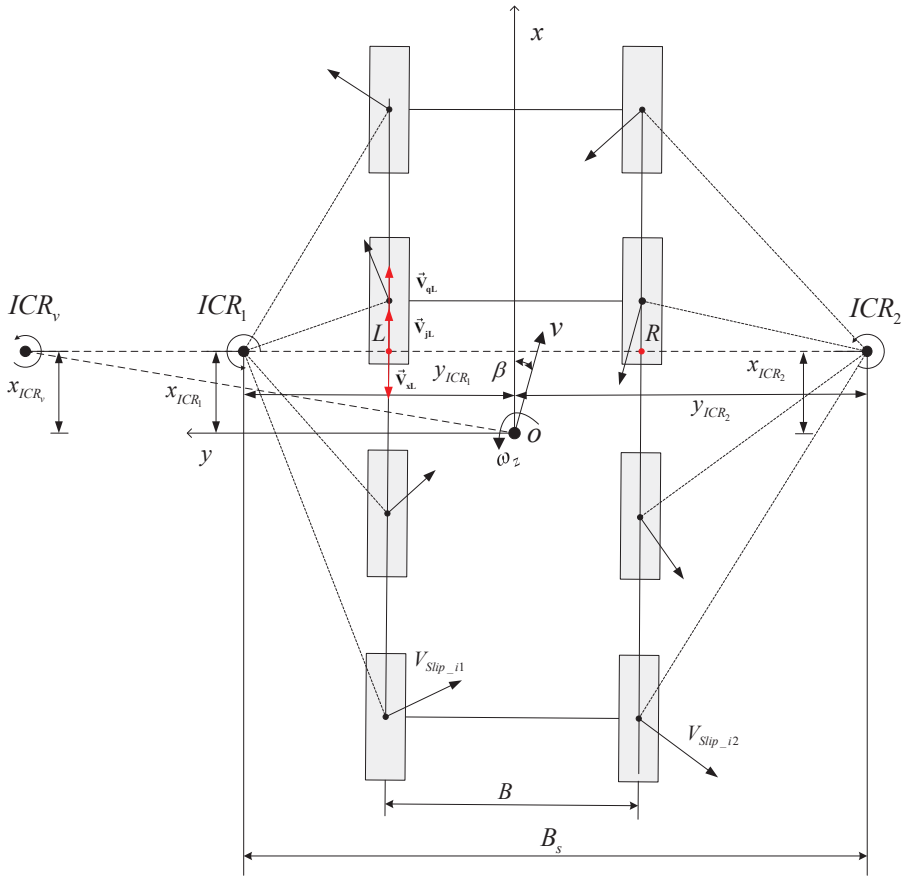


Figure 2. The ICRs of multi-axis skid-steered wheeled vehicles.

The turning radius R_s of the vehicle can be determined using the coordinates of the instantaneous turning center. The specific expression is

$$R_s = \sqrt{{x_{ICR_v}}^2 + {y_{ICR_v}}^2}. \tag{7}$$

2.4. SD-Based Linear 2-DOF Dynamics Model of Skid-Steered Wheeled Vehicle

Assuming that during the steering process, the rotational speeds of the wheels on the same side are equal, the wheel speed inputs for each degree of freedom on a single side are simplified into a single input:

$$\begin{cases} \omega_{t11} = \cdots = \omega_{tn1} = \omega_{t1} \\ \omega_{t12} = \cdots = \omega_{tn2} = \omega_{t2} \end{cases}, \tag{8}$$

where ω_{tij} represents the rotational speed of each wheel. Using the SD between the left and right wheels as the steering input, the expression is

$$\Delta u = R_t \Delta\omega_t = R_t(\omega_{t2} - \omega_{t1}). \tag{9}$$

Without considering the influence of the vehicle's longitudinal motion, substituting the above formula into Equation (1) yields the SD-based linear 2-DOF model.

$$\begin{cases} m(\dot{v}_y + v_x\omega_z) = \frac{2\sum_{i=1}^{n} K_{\alpha i}}{v_x} v_y + \frac{2\sum_{i=1}^{n} L_i K_{\alpha i}}{v_x}\omega_z \\ I_z\dot{\omega}_z = \frac{2\sum_{i=1}^{n} L_i K_{\alpha i}}{v_x} v_y + \left(\frac{2\sum_{i=1}^{n} L_i^2 K_{\alpha i}}{v_x} - \frac{B^2\sum_{i=1}^{n} K_{xi}}{2v_x} \right)\omega_z + \frac{B\sum_{i=1}^{n} K_{xi}}{2} \cdot \frac{\Delta u}{v_x} \end{cases}, \tag{10}$$

where K_{xi} represents the longitudinal stiffness; $K_{\alpha i}$ represents the cornering stiffness.

Based on $\beta = v_y/v_x$, transform Equation (10) into a state-space expression in terms of β and ω_z about $\Delta u/v_x$ as input:

$$\begin{bmatrix} \dot{\beta} \\ \dot{\omega}_z \end{bmatrix} = \begin{bmatrix} \frac{2\sum_{i=1}^{n} K_{\alpha i}}{mv_x} & \frac{2\sum_{i=1}^{n} L_i K_{\alpha i}}{mv_x^2} - 1 \\ \frac{2\sum_{i=1}^{n} L_i K_{\alpha i}}{I_z} & \frac{4\sum_{i=1}^{n} L_i^2 K_{\alpha i} - B^2\sum_{i=1}^{n} K_{xi}}{2I_z v_x} \end{bmatrix} \begin{bmatrix} \beta \\ \omega_z \end{bmatrix} + \begin{bmatrix} 0 \\ \frac{B\sum_{i=1}^{n} K_{xi}}{2I_z} \end{bmatrix} \frac{\Delta u}{v_x}. \tag{11}$$

Applying the Laplace transform to Equation (11), the first-order transfer functions for β and in terms of the control input $\Delta u/v_x$ can be solved as follows:

$$\begin{bmatrix} \frac{\beta(s)}{\frac{\Delta u}{v_x}(s)} \\ \frac{\omega_z(s)}{\frac{\Delta u}{v_x}(s)} \end{bmatrix} = \frac{\begin{bmatrix} s - \frac{4\sum_{i=1}^{n} L_i^2 K_{\alpha i} - B^2\sum_{i=1}^{n} K_{xi}}{2I_z v_x} & \frac{2\sum_{i=1}^{n} L_i K_{\alpha i}}{mv_x^2} - 1 \\ \frac{2\sum_{i=1}^{n} L_i K_{\alpha i}}{I_z} & s - \frac{2\sum_{i=1}^{n} K_{\alpha i}}{mv_x} \end{bmatrix} \begin{bmatrix} 0 \\ \frac{B\sum_{i=1}^{n} K_{xi}}{2I_z} \end{bmatrix}}{s^2 - \frac{4I_z\sum_{i=1}^{n} K_{\alpha i} + 4m\sum_{i=1}^{n} L_i^2 K_{\alpha i} - mB^2\sum_{i=1}^{n} K_{xi}}{2I_z m v_x} s + \frac{4\sum_{i=1}^{n} L_i^2 K_{\alpha i}\sum_{i=1}^{n} K_{\alpha i} - 4\left(\sum_{i=1}^{n} L_i K_{\alpha i}\right)^2 + 2mv_x^2\sum_{i=1}^{n} L_i K_{\alpha i} - B^2\sum_{i=1}^{n} K_{\alpha i}\sum_{i=1}^{n} K_{xi}}{I_z m v_x^2}}. \tag{12}$$

In steady-state conditions, setting the Laplace operator s = 0 in Equation (12), solve for the steady-state gain of the vehicle's center of mass side-slip angle and the yaw rate gain with respect to the steering input $\Delta u/v_x$:

$$\begin{cases} \left.\frac{\beta}{\frac{\Delta u}{v_x}}\right|_{s=0} = \frac{B\sum_{i=1}^{n} K_{xi}\left(2\sum_{i=1}^{n} L_i K_{\alpha i} - mv_x^2\right)}{8\sum_{i=1}^{n} L_i^2 K_{\alpha i}\sum_{i=1}^{n} K_{\alpha i} - 8\left(\sum_{i=1}^{n} L_i K_{\alpha i}\right)^2 + 4mv_x^2\sum_{i=1}^{n} L_i K_{\alpha i} - 2B^2\sum_{i=1}^{n} K_{\alpha i}\sum_{i=1}^{n} K_{xi}} \\ \left.\frac{\frac{\omega_z}{\Delta u}}{v_x}\right|_{s=0} = \frac{-v_x B\sum_{i=1}^{n} K_{\alpha i}\sum_{i=1}^{n} K_{xi}}{4\sum_{i=1}^{n} L_i^2 K_{\alpha i}\sum_{i=1}^{n} K_{\alpha i} - 4\left(\sum_{i=1}^{n} L_i K_{\alpha i}\right)^2 + 2mv_x^2\sum_{i=1}^{n} L_i K_{\alpha i} - B^2\sum_{i=1}^{n} K_{\alpha i}\sum_{i=1}^{n} K_{xi}} \end{cases}. \quad (13)$$

Referring to the expression for the steady-state yaw rate gain in Ackermann steering, transform Equation (13) into

$$\left.\frac{\omega_z}{\Delta u / v_x}\right)_{s=0} = \frac{A_\omega v_x}{C_\omega + D_\omega {v_x}^2}, \quad (14)$$

where, $A_\omega = -B\sum_1^n K_{\alpha i}\sum_1^n K_{xi}$, $C_\omega = 4\sum_1^n {L_i}^2 K_{\alpha i}\sum_1^n K_{\alpha i} - 4(\sum_1^n L_i K_{\alpha i})^2 - B^2\sum_1^n K_{\alpha i}\sum_1^n K_{xi}$, $D_\omega = 2m\sum_1^n L_i K_{\alpha i}$.

For the steering input $\Delta u / v_x$, the stability factor can be defined as $K_\omega = D_\omega / C_\omega$. Since C_ω is always positive, the sign of D_ω will determine the vehicle's steering characteristics. Similar to Ackermann steering, when $D_\omega > 0$, the vehicle exhibits understeering (US) characteristics; when $D_\omega = 0$, the vehicle exhibits neutral steering (NS) characteristics; and when $D_\omega < 0$, the vehicle exhibits oversteering (OS) characteristics.

For the analysis of the steady-state ICR, set $\dot{\beta} = 0$ and substitute $\dot{\omega}_z = 0$ into Equation (10). According to Equation (6), the coordinates of the vehicle's instantaneous turning center can be solved:

$$\begin{cases} x_{ICR_v} = -\frac{v_y}{\omega_z} = \frac{2\sum_{i=1}^{n} L_i K_{\alpha i} - mv_x^2}{2\sum_{i=1}^{n} K_{\alpha i}} \\ y_{ICR_v} = \frac{v_x}{\omega_z} = B\frac{v_x}{\Delta u}\left[1 - \frac{4\sum_{i=1}^{n} L_i^2 K_{\alpha i}\sum_{i=1}^{n} K_{\alpha i} + 2mv_x^2\sum_{i=1}^{n} L_i K_{\alpha i} - 4\left(\sum_{i=1}^{n} L_i K_{\alpha i}\right)^2}{B^2\sum_{i=1}^{n} K_{\alpha i}\sum_{i=1}^{n} K_{xi}}\right] \end{cases}. \quad (15)$$

3. TD-Based Linear 2-DOF Dynamics Model of a Skid-Steered Wheeled Vehicle

From Equation (1), it is evident that compared to the single-track "bicycle model", the equation describing the yaw motion includes a term representing the yaw moment generated by the longitudinal forces of the tires on both sides: $B\sum_1^n (F_{txi2} - F_{txi1})/2$. This term is considered the cause of steering in differential steering vehicles.

Based on the single-wheel dynamics model in Equation (4), when the vehicle is in steady-state turning, the wheel angular acceleration $\dot{\omega}_{tij} = 0$. Therefore, the relationship between the wheel driving torque and the longitudinal force can be obtained:

$$T_{tij} = F_{tzij}\Delta_{ij} + F_{txij}R_t. \quad (16)$$

Define the torque difference between the sides as

$$\Lambda T = \sum_1^4 T_{i2} - T_{i1} = R_t\sum_1^4 F_{xi2} - F_{xi1}, \quad (17)$$

where ΛT represents the torque produced by the drive system and amplified through the transmission to become the driving torque on the wheel.

Based on the TD between the sides and combining it with Equation (1), establish a skid-steered wheeled vehicle model with torque difference $\Delta T / R_t$ as the steering input:

$$\begin{cases} m\left(\dot{v}_y + v_x\omega_z\right) = \frac{2\sum_{i=1}^{n} K_{\alpha i}}{v_x} v_y + \frac{2\sum_{i=1}^{n} L_i K_{\alpha i}}{v_x}\omega_z \\ I_z\dot{\omega}_z = \frac{B}{2}\cdot\frac{\Delta T}{R_t} + \frac{2\sum_{i=1}^{n} L_i K_{\alpha i}}{v_x} v_y + \frac{2\sum_{i=1}^{n} L_i^2 K_{\alpha i}}{v_x}\omega_z \end{cases}. \tag{18}$$

Based on $\beta = v_y/v_x$, transform Equation (18) into a state-space expression in terms of β and ω_z with respect to the $\Delta T/R_t$ input:

$$\begin{bmatrix} \dot{\beta} \\ \dot{\omega}_z \end{bmatrix} = \begin{bmatrix} \frac{2\sum_{i=1}^{n} K_{\alpha i}}{mv_x} & \frac{2\sum_{i=1}^{n} L_i K_{\alpha i}}{mv_x^2} - 1 \\ \frac{2\sum_{i=1}^{n} L_i K_{\alpha i}}{I_z} & \frac{2\sum_{i=1}^{n} L_i^2 K_{\alpha i}}{I_z v_x} \end{bmatrix} \begin{bmatrix} \beta \\ \omega_z \end{bmatrix} + \begin{bmatrix} 0 \\ \frac{B}{2I_z} \end{bmatrix} \frac{\Delta T}{R_t}. \tag{19}$$

3.1. Steady-State Characteristics Analysis

By applying the Laplace transform to Equation (19), the first-order transfer functions for β and ω_z with respect to the control input $\Delta T/R_t$ can be solved:

$$\begin{bmatrix} \frac{\beta(s)}{\frac{\Delta T}{R_t}(s)} \\ \frac{\omega_z(s)}{\frac{\Delta T}{R_t}(s)} \end{bmatrix} = \frac{\begin{bmatrix} s - \frac{2\sum_{i=1}^{n} L_i^2 K_{\alpha i}}{I_z v_x} & \frac{2\sum_{i=1}^{n} L_i K_{\alpha i}}{mv_x^2} - 1 \\ \frac{2\sum_{i=1}^{n} L_i K_{\alpha i}}{I_z} & s - \frac{2\sum_{i=1}^{n} K_{\alpha i}}{mv_x} \end{bmatrix} \begin{bmatrix} 0 \\ \frac{B}{2I_z} \end{bmatrix}}{s^2 - \frac{2I_z\sum_{i=1}^{n} K_{\alpha i} + 2m\sum_{i=1}^{n} L_i^2 K_{\alpha i}}{I_z m v_x} s + \frac{4\sum_{i=1}^{n} L_i^2 K_{\alpha i}\sum_{i=1}^{n} K_{\alpha i} - 4\left(\sum_{i=1}^{n} L_i K_{\alpha i}\right)^2 + 2mv_x^2\sum_{i=1}^{n} L_i K_{\alpha i}}{I_z m v_x^2}}. \tag{20}$$

In steady-state conditions, setting s = 0 in Equation (20), solve for the steady-state yaw rate gain and the center of mass side-slip angle gain with respect to the steering input $\Delta u/v_x$.

$$\begin{cases} \left.\frac{\beta}{\frac{\Delta T}{R_t}}\right|_{s=0} = \frac{B\left(2\sum_{i=1}^{n} L_i K_{\alpha i} - mv_x^2\right)}{8\sum_{i=1}^{n} L_i^2 K_{\alpha i}\sum_{i=1}^{n} K_{\alpha i} - 8\left(\sum_{i=1}^{n} L_i K_{\alpha i}\right)^2 + 4mv_x^2\sum_{i=1}^{n} L_i K_{\alpha i}} \\ \left.\frac{\omega_z}{\frac{\Delta T}{R_t}}\right|_{s=0} = \frac{-v_x B\sum_{i=1}^{n} K_{\alpha i}}{4\sum_{i=1}^{n} L_i^2 K_{\alpha i}\sum_{i=1}^{n} K_{\alpha i} - 4\left(\sum_{i=1}^{n} L_i K_{\alpha i}\right)^2 + 2mv_x^2\sum_{i=1}^{n} L_i K_{\alpha i}} \end{cases}. \tag{21}$$

Then, the steady-state yaw rate gain can be described as

$$\left.\frac{\omega_z}{\Delta T/R_t}\right)_{s=0} = \frac{A_T v_x}{C_T + D_T {v_x}^2}, \tag{22}$$

where, $A_T = -B\sum_1^n K_{\alpha i}$, $C_T = 4\sum_1^n L_i{}^2 K_{\alpha i}\sum_1^n K_{\alpha i} - 4(\sum_1^n L_i K_{\alpha i})^2$, $D_T = 2m\sum_1^n L_i K_{\alpha i}$.

For the steering input $\Delta T/R_t$, define the stability factor as $K_T = D_T/C_T$. Since C_T is always positive, the sign of D_T will determine the vehicle's steering characteristics. Similar to Ackermann steering, when $D_T > 0$, the vehicle exhibits US characteristics; when $D_T = 0$, the vehicle exhibits NS characteristics; and when $D_T < 0$, the vehicle exhibits OS characteristics.

Figure 3 shows the steady-state yaw rate gain and side slip angle gain for skid-steered wheeled vehicles. For US vehicles, the steady-state yaw rate gain initially increases and once the characteristic speed is reached, the steady-state yaw rate gain begins to drop. The variation ranges of both the steady-state yaw rate gain and the side slip angle gain are relatively small, indicating a relatively stable steering mode, although it lacks flexibility and is less prone to oversteering and excessive side slip. For NS vehicles, both gains vary linearly with vehicle speed. For OS vehicles, the absolute values of both gains increase as the vehicle speed rises. When the speed approaches the characteristic speed, both gains

approach infinity, suggesting that even a minimal TD input can induce an extremely small turning radius, leading the vehicle to oversteer and exhibit excessive side slip.

Using Equation (18), the coordinates of the ICR in the lateral and longitudinal directions can be determined for the case of steady-state steering with respect to the $\Delta T / R_t$ input.

$$\begin{cases} x_{ICR_v} = -\frac{v_y}{\omega_z} = \frac{2\sum_1^n L_i K_{\alpha i} - m v_x^2}{2\sum_1^n K_{\alpha i}} \\ y_{ICR_v} = \frac{v_x}{\omega_z} = \frac{R_t}{\Delta T}\left[\frac{4\left(\sum_1^n L_i K_{\alpha i}\right)^2 - 4\sum_1^n L_i^2 K_{\alpha i}\sum_1^n K_{\alpha i} - 2m v_x^2 \sum_1^n L_i K_{\alpha i}}{B\sum_1^n K_{\alpha i}}\right] \end{cases} . \quad (23)$$

From Equation (23), it can be seen that the longitudinal ICR of a skid-steered vehicle is independent of the steering input. Regardless of the type of steering input used, the expression for the longitudinal coordinate of the ICR remains unchanged.

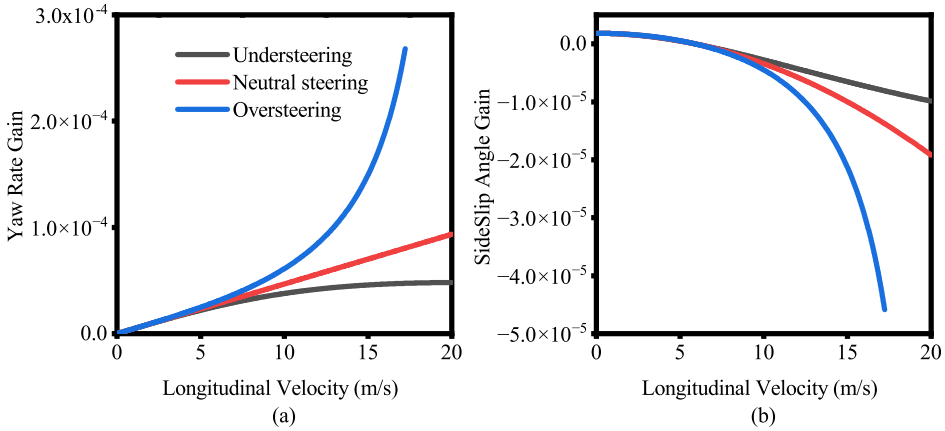


Figure 3. (**a**) The relationship between steady-state yaw rate gain and speed under different steering characteristics. (**b**) The relationship between steady-state side slip angle gain and speed under different steering characteristics.

As depicted in Figure 4a, the longitudinal ICR remains independent of the steering input. As vehicle velocity increases, a consistent trend emerges across all steering types, showing the ICR advancing forward. With increasing speed, the centripetal force required to maintain a given yaw rate also escalates, necessitating additional wheel contribution for generating the necessary centripetal force. At lower speeds, the lateral forces exerted by the front axles point away from the turning center, indicating that these forces do not contribute to the centripetal force. Once the ICR surpasses the first axle, all wheels begin to assist in generating this force. Concurrently, as the ICR advances, the side slip angle of each tire amplifies, progressively compromising vehicle stability. Moreover, the rate at which the ICR exits the vehicle's boundary is most significant in US vehicles, underscoring their enhanced stability. Figure 4b illustrates that for US vehicles, the lateral ICR escalates with increasing velocity, suggesting that the turning radius enlarges at higher speeds for the same steering input. Conversely, for OS vehicles, the opposite trend is observed. For NS vehicles, the lateral steering center remains constant, and the steering radius diminishes with increased steering input.

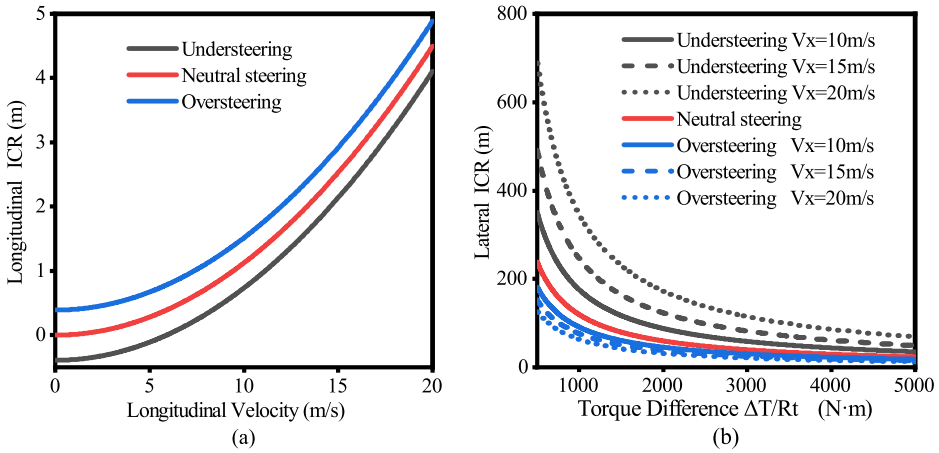


Figure 4. (**a**) The relationship between the longitudinal coordinates of the ICR, velocity, and steering characteristics. (**b**) The relationship between the lateral coordinates of the ICR, velocity, and steering characteristics and torque differential input.

3.2. Instantaneous-State Characteristics Analysis

If the denominator term in Equation (20) is expressed as a characteristic equation, then its natural frequency and damping ratio can be derived as

$$\begin{cases} \omega_0 = \sqrt{\frac{C_T + D_T v_x^2}{I_z m v_x^2}} \\ \xi = -\frac{I_z \sum_1^n K_{\alpha i} + m \sum_1^n L_i^2 K_{\alpha i}}{I_z m v_x \omega_0} \end{cases}. \tag{24}$$

Figure 5 shows the relationship between the characteristic parameters of the TD-based 2-DOF Model and velocity. Similar to Ackermann steering vehicles, US, NS, and OS correspond to underdamped, critically damped, and overdamped states, respectively. Analyzing the stability criteria of the second-order characteristic equation, for underdamped and critically damped states, the vehicle always exhibits stability. In contrast, for the overdamped state, the vehicle exhibits oversteering characteristics, and when velocity increases to a certain extent, the characteristic $\omega_0{}^2$ become negative, indicating instability.

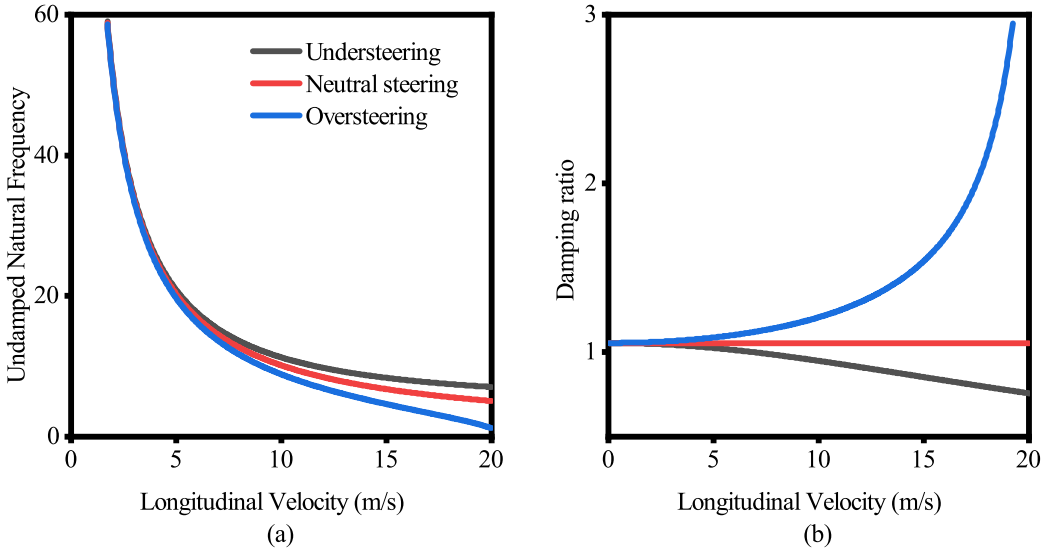


Figure 5. (**a**) The relationship between undamped natural frequency of the TD-based 2-DOF model and velocity under different steer characteristics. (**b**) The relationship between damping ratio of the TD-based 2-DOF model and velocity under different steer characteristics.

Employing Equation (24), the time-domain response characteristics of ω_z and β under a step input of a 3000 N·m torque differential at $v_x = 10$ m/s, $v_x = 15$ m/s, and $v_x = 20$ m/s can be calculated.

Figure 6a shows the time-domain response characteristics of ω_z. As velocity increases, the time-domain responses of ω_z for various steering behaviors below the characteristic speed tend to rise. Vehicles exhibiting US show progressively increasing overshoots, whereas those with NS respond faster, and OS responses slow down. Concerning response magnitude, US vehicles display smaller values, while OS vehicles demonstrate the largest responses, aligning with earlier analyses of steady-state ω_z gains. Figure 6b presents the time-domain response of β. The absence of a first-order term in the transfer function's numerator Equation (23) prevents any overshoot in this response.

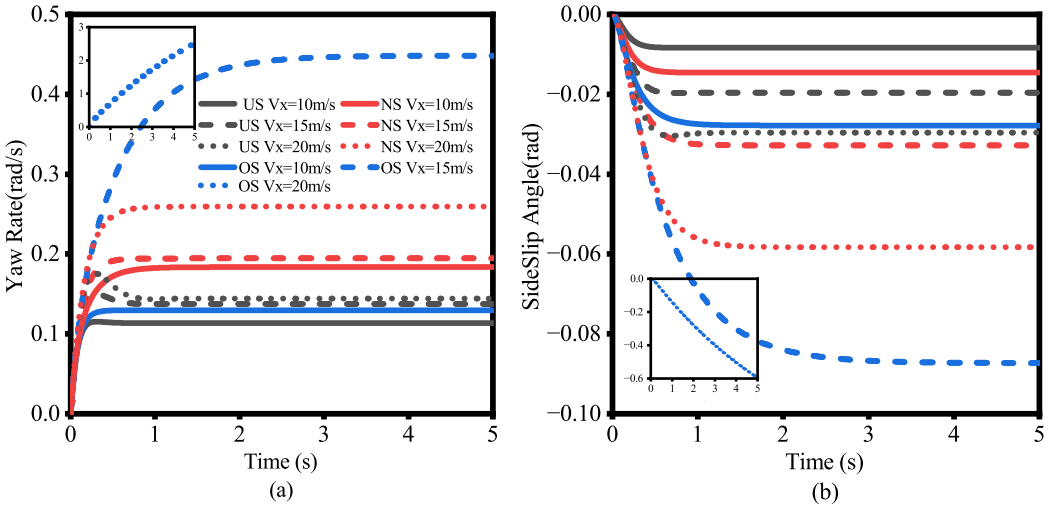


Figure 6. (**a**) The time-domain response characteristics of yaw rate under a step input of a 3000 N·m torque differential under different steer characteristics and velocities. (**b**) The time-domain response characteristics of side slip angle under the same conditions.

Figure 7 illustrates the frequency-domain responses of various steering behaviors. As previously noted, vehicles with excessive steering at near $v_x = 20$ m/s instability; hence, the frequency-domain response characteristics are not further analyzed under this condition. Regarding amplitude ratio parameters, the steering process requires a substantial TD to counteract ground resistance, yielding minimal amplitude ratios at near-zero frequencies. As velocity increases, the capacity to maintain uniform gain across all frequencies decreases, yet US vehicles tend to sustain more stable amplitude ratios. Analysis of phase angle parameters indicates significant speed influence, with higher velocity causing more pronounced changes and clear phase distortion. Under comparable conditions, US vehicles display smaller fluctuations in both ω_z and β phase angles, suggesting less phase distortion and a faster response to achieve steady-state values.

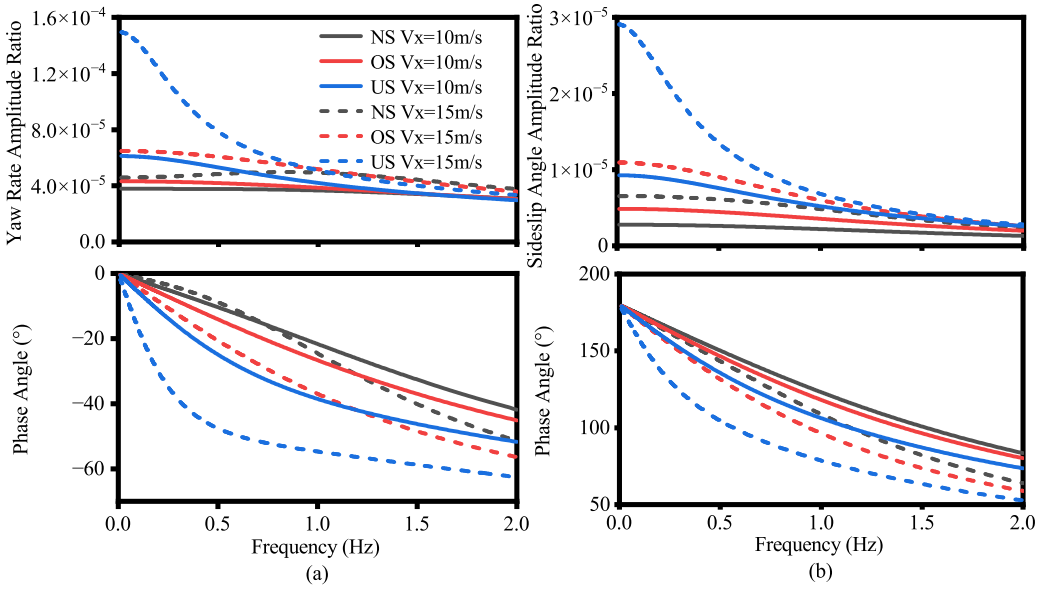


Figure 7. (**a**) The frequency-domain response characteristics of yaw rate under a step input of a 3000 N·m torque differential under different steer characteristics and velocities. (**b**) The frequency-domain response characteristics of side slip angle under the same conditions.

4. Real Vehicle Test Result

To verify the dynamic performance of the proposed 2-DOF model, real vehicle testing is conducted to validate model accuracy. Verification metrics include the vehicle's turning radius and the tracking of lateral motion parameters during steering maneuvers. Maintaining a constant steering wheel angle and vehicle speed is challenging due to the difficulty of ensuring that all driver operations precisely match predefined conditions. Consequently, a validation approach combining experimentation with subsequent simulation is adopted. Collected steering inputs are utilized for the 2-DOF model, and the resulting calculated curves are compared with actual curves for verification.

4.1. Experimental Platform Introduction

The experimental platform is an electric-driven 8 × 8 skid-steered wheeled vehicle. Compared to traditional hydraulically and mechanically driven skid-steered vehicles, electric drive systems provide a faster response, smoother power delivery, and more precise control, which can also swiftly track driver inputs, reducing latency in steering commands. The mechanical structure of electric drive systems is simpler, minimizing energy losses caused by mechanical transmissions. Most importantly, electric drive systems eliminate the need for additional sensors, as essential data such as rotational speed and torque can be directly obtained from the motor controller. This integration streamlines system architecture and ensures precise, reliable data acquisition for control and analysis.

The drive system of the platform includes two sets of drive motors and corresponding transmission devices. Two driving motors are installed on the two sides of the vehicle body to drive the four wheels on the same side by transmission. The torque is given by the motor controller and the speed is given by the encoder. The motion speed of the wheel on the same side is the same because of the mechanical structure of the drive system. The relevant data can be directly obtained from the motor controller. Integrating these data with the vehicle's drive schematic allows for precise computation of speed and torque differentials between the left and right wheels during operation. The essential parameters of the platform are shown in Table 1.

Table 1. Vehicle parameter.

Parameters	Symbols	Numeric Values	Units
Vehicle mass	m	2850	kg
Length of the vehicle	L	3900	mm
Width of the vehicle	B	1800	mm
Moment of inertia around z-axis	I_z	2300	kg·m^2
Distance between each axis	$L_{12} \times L_{23} \times L_{34}$	765 × 765 × 765	mm
Distance between 1st axis to center of mass	L_1	1305	mm
Height of center of mass	h	510	mm
Max engine power	$P_{e\max}$	80	kW
Max engine Torque	$T_{e\max}$	320	N·m
Tranmission rate	$i_e \times i_{wheel}$	7.869 × 1.933	-
Radius of the tire	R_t	0.31	m

Additionally, a GPS-IMU combined navigation system is utilized to collect trajectory and acceleration data, as detailed in Figure 8. The navigation system includes the IMU, GPS, and dual antennas corresponding to the GPS. The IMU provides the acceleration and rotation rate on the three axes. The dual antenna is located on the axle wire of the UGV. The RTK-GPS can provide accurate longitude and lateral velocity, position, and direction information.

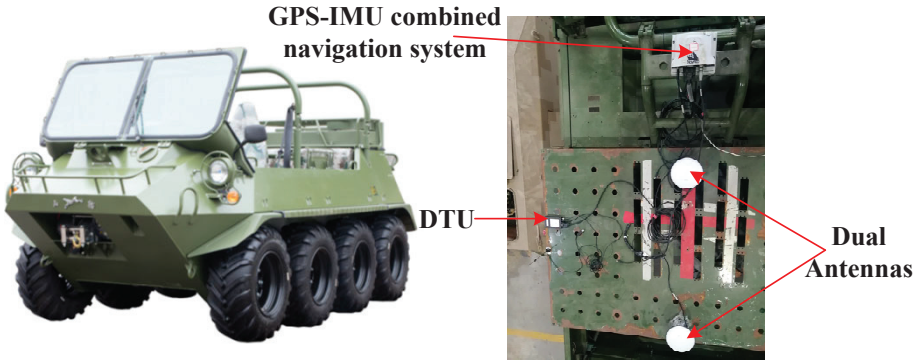


Figure 8. GPS-IMU combined navigation system.

4.2. Steering Radius Test

In the steering radius test, the driver applies steering inputs at speeds of $v_x = 12.5$ m/s, $v_x = 10$ m/s, and $v_x = 7.5$ m/s. The actual turning radius is calculated using Equation (7) and motion data from the integrated navigation system. The steering radii are calculated using Equations (15) and (23), and these values are compared with actual measurements to validate the model accuracy. Owing to the size constraints of the test site, fixed steering inputs cannot be maintained for extended periods. Consequently, the driver holds the steering input briefly to simulate a quasi-steady-state turning process. Only experimental data from periods of stable steering input are used to calculate the turning radius, facilitating the validation of the two models.

Figure 9 depicts the steering inputs and calculated turning radius at various velocity. Steering radius calculations were based on segments with relatively stable steering inputs to ensure reliability. Due to variations in driver skill and operational stability, steering inputs may not always remain stable. However, the electric drive system's rapid response capabilities enable quick tracking of the driver's steering intentions, producing step responses in steering. Figure 9a shows that the high signal-to-noise ratio of the SD input leads to significant fluctuations in the calculated radius with the SD-based model. Despite this,

the calculated results align with the actual steering radius trends. Moreover, the TD-based model, characterized by a larger magnitude and smaller signal-to-noise ratio, produces calculated radii with fewer fluctuations, smoother trends, and greater consistency with actual data.

Error analysis from Figure 9b shows average relative errors of 10.232%, 8.16%, and 7.594% for the three operating conditions under the SD-based model. For the TD-based model, average relative errors are 6.315%, 6.509%, and 5.503%, respectively. A comprehensive comparison of these tests indicates that the TD-based 2-DOF model calculates the radius with minimal fluctuations and relatively low errors. Furthermore, both theoretical models correspond well with the experimental data, suggesting that the formulas for calculating the turning radius achieve a satisfactory level of accuracy.

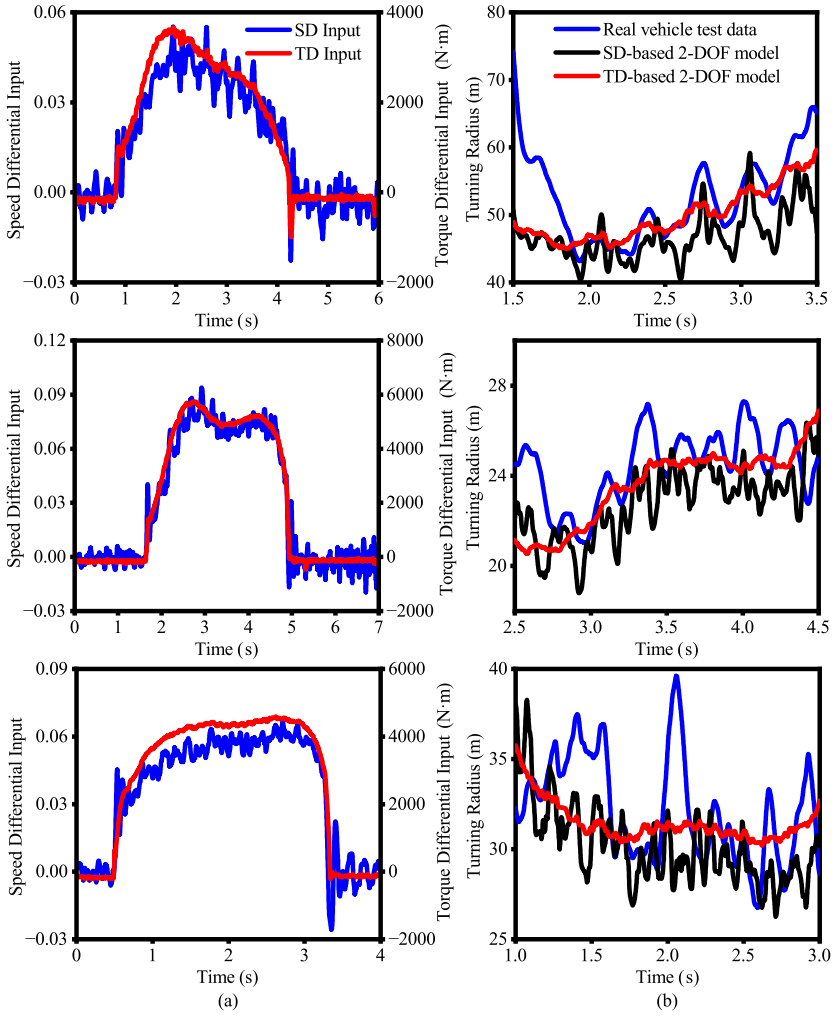


Figure 9. (**a**) The steer inputs of SD and TD under the speed of 12.5 m/s, 10 m/s, and 7.5 m/s. (**b**) Comparison of actual and calculated turning radius under the speed of 12.5 m/s, 10 m/s, and 7.5 m/s.

4.3. Steering Step Response Experiment

During transient characteristic testing of vehicle steering, the same experimental platform validated the model's dynamic characteristics using step and pulse inputs to the steering wheel.

In the steering step input test, the driver quickly turns the steering wheel to a predetermined angle, holds it briefly, and then returns it to the original position. Data collected from the drive motors and vehicle speed are integrated as TD and SD inputs. These inputs

are processed by the aforementioned 2-DOF models, and the resulting curves are compared with the actual data. In the real vehicle step response experiment, the steering conditions from the turning radius analysis were replicated to simulate step responses. Step steering inputs were applied at $v_x = 12.5$ m/s, $v_x = 10$ m/s, and $v_x = 7.5$ m/s. Using both models, the step responses of the vehicle for ω_z, a_y, and β were calculated and then compared with data from the integrated navigation system to validate the precision.

Figure 10 compares the step response characteristics of the two models under varying velocities with actual data, which demonstrates that the two models effectively track the vehicle's step steering inputs. However, the calculated step responses are consistently lower than the actual vehicle responses, exhibiting longer rise and return times. This discrepancy arises from the linear models' simplifications, which overlook complex operational factors, thus yielding lower-amplitude step responses than observed in real conditions. Comparison of the two models reveals that the TD-based model responds more sensitively to step inputs, exhibiting shorter delays in both rise and return times. Both models show similar step response amplitudes, though the TD-based model exhibits slightly higher amplitudes than its SD-based counterpart.

4.4. Steering Impulse Response Experiment

The vehicle's steering response to impulse inputs displays pronounced transient characteristics, enabling a more detailed evaluation of the two proposed models. In the impulse steering test, the driver rapidly turns the steering wheel to a predetermined angle and then swiftly centers it. This process is repeated, causing the vehicle to undergo multiple quick directional changes and recoveries in rapid succession.

In this study, multiple impulse steering inputs were applied continuously at $v_x = 8$ m/s, $v_x = 10$ m/s, and $v_x = 12$ m/s. The step responses of the ω_z, a_y, and β were calculated using both models and compared with the real vehicle data to validate the accuracy of the two models. During the experiment, inertia causes an overshoot when the steering wheel returns to its neutral position, which prevents the steering input from returning precisely to zero, resulting in a transient reverse impulse response. The overshoot of the steering wheel angle is significant for analyzing the impulse response conditions discussed, enabling evaluation of how effectively the two models track instantaneous reverse changes in steering input.

Figure 11 illustrates that the two models exhibit similar response characteristics under both impulse and step inputs. Both models accurately track steering inputs, displaying distinct ω_z, a_y, and β impulse responses. While the bandwidth aligns with actual inputs, the response amplitudes are smaller, and the absolute errors larger, compared to those in step steering conditions. Impulse responses involve high-magnitude, instantaneous inputs, accentuating the system's high-frequency response. These transient inputs expose the nonlinear characteristics of the tires, resulting in more pronounced errors in ω_z, a_y, and β measurements under impulse conditions compared to step inputs. Comparison of the response characteristics of two models confirms earlier findings: the TD-based linear 2-DOF model more effectively tracks the vehicle's steering inputs and better handles the overshoot during steering wheel return. Conversely, the SD-based model fails to fully capture changes in steering input during the return phase, exhibiting a slower response and inferior tracking of the overshoot phenomenon compared to the TD-based model. Additionally, error analysis conducted from the onset to the end of the impulse response indicates that the TD-based 2-DOF model demonstrates a smaller average relative error during the step response phase. However, the amplitude response accuracy of the two models shows no significant differences.

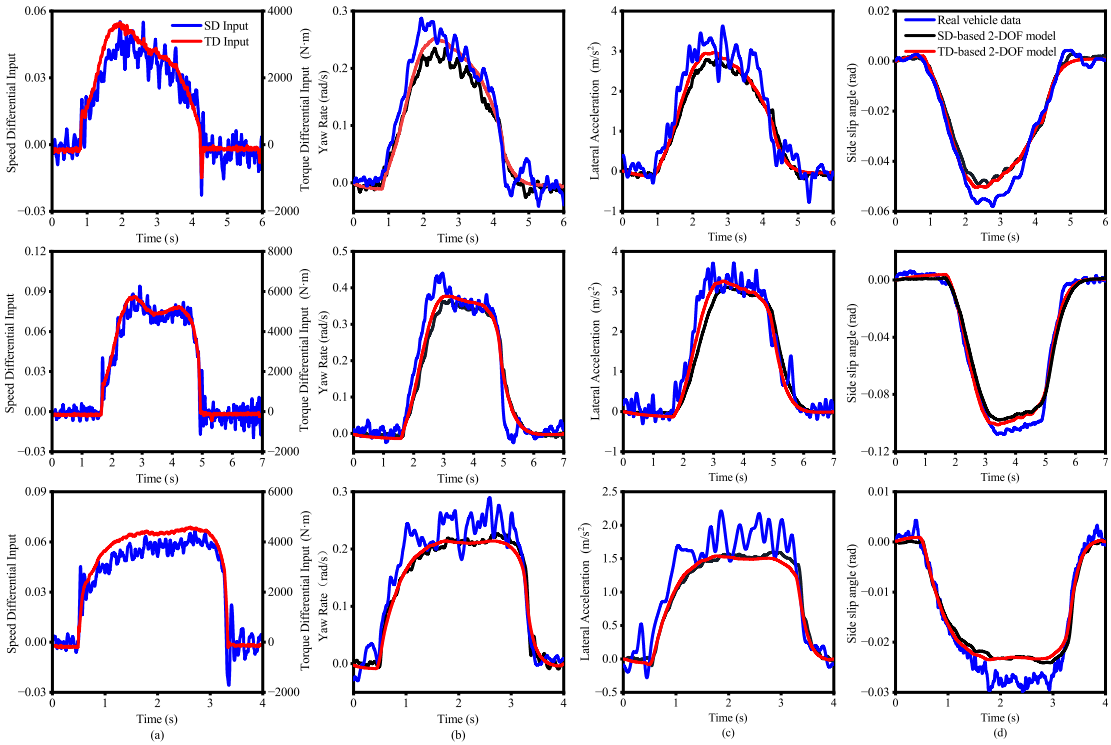


Figure 10. (**a**) The step steer inputs of SD and TD under the speeds of 12.5 m/s, 10 m/s, and 7.5 m/s. (**b**) Comparison of actual and calculated yaw rate step response under the speeds of 12.5 m/s, 10 m/s, and 7.5 m/s. (**c**) Comparison of actual and calculated lateral acceleration step response under the speeds of 12.5 m/s, 10 m/s, and 7.5 m/s. (**d**) Comparison of actual and calculated side slip angle step response under the speeds of 12.5 m/s, 10 m/s, and 7.5 m/s.

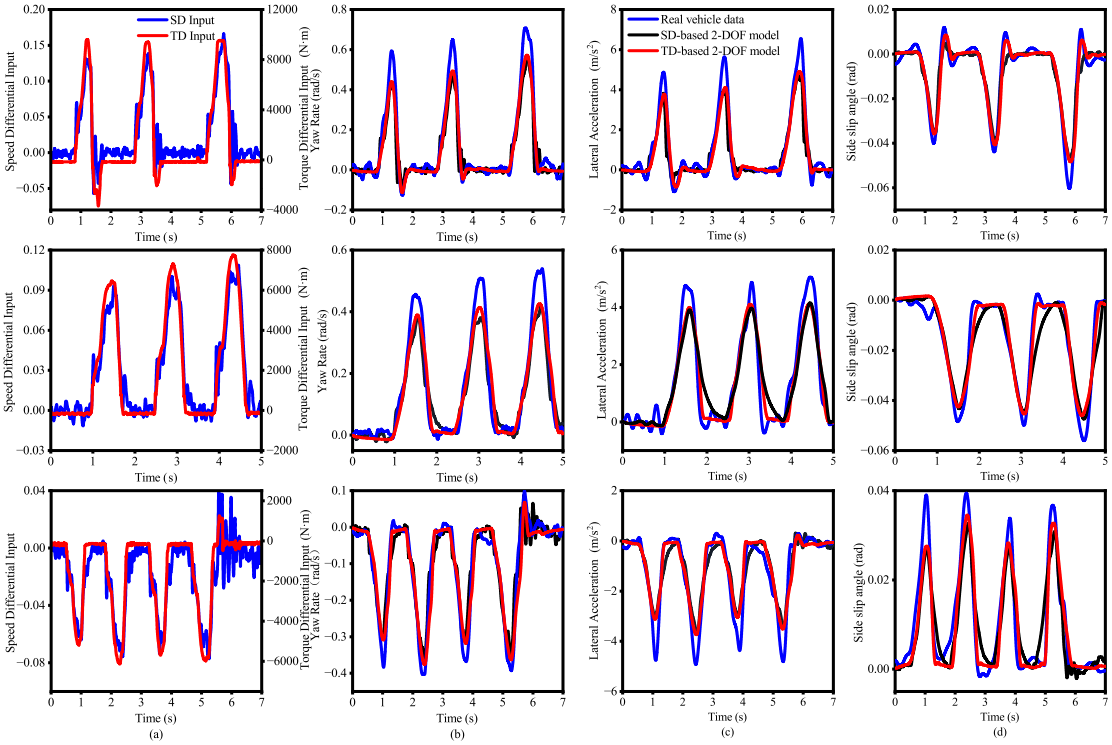


Figure 11. (**a**) The impulse steer inputs of SD and TD under the speeds of 8 m/s, 10 m/s, and 12 m/s. (**b**) Comparison of actual and calculated yaw rate impulse response under the speeds of 8 m/s, 10 m/s, and 12 m/s. (**c**) Comparison of actual and calculated lateral acceleration impulse response under the speeds of 8 m/s, 10 m/s, and 12 m/s. (**d**) Comparison of actual and calculated side slip angle impulse response under the speeds of 8 m/s, 10 m/s, and 12 m/s.

5. Discussion

The research focus of this paper is on the dynamic modeling and steering characteristics of skid-steered wheeled vehicle. The fundamental cause of steering in skid-steered wheeled vehicles is the torque difference between the left and right drive wheels; then, the TD-based 2-DOF dynamics model was developed. The steady- and instantaneous-state steering characteristics were analyzed based the model. Comparative experiments with real vehicle tests demonstrate that the TD-based linear 2-DOF model exhibits superior accuracy in calculating steady-state steering radii, responds more swiftly to varied frequency steering inputs, and partially tracks the overshoot during steering wheel return. Additionally, the model maintains high precision in amplitude responses, albeit with a noticeable reduction in accuracy under high-frequency steering inputs. Combining step response and impulse response analyses, the TD-based model outperforms under high-frequency steering inputs, though both models perform well with mid-to-low frequency inputs. Within an acceptable error margin, both models adequately describe the steering responses under these conditions. In the model development process, the effect of longitudinal velocity on steering dynamics was deliberately excluded to prioritize the analysis of steering characteristics and derive general conclusions. This simplification limits the model's real-world applicability, as longitudinal velocity significantly affects vehicle dynamics, particularly tire slip and overall handling performance. The longitudinal velocity variation should be integrated into the model to offer a more comprehensive understanding of the vehicle's steering dynamics and stability.

Future research will explore the practical application of the TD-based linear 2-DOF model and SD-based model in the steering control of skid-steered wheeled vehicles. This will include the integration of these models into advanced steering control systems and analysis of their response characteristics under varying steering input conditions, with a comprehensive assessment of their robustness and reliability in dynamic and unpredictable environments. Moreover, the comparison between TD-based and SD-based models should extend beyond system response analysis. It is equally important to assess the impact of different steering inputs on the overall energy consumption of the vehicle. Such analysis could lead to the development of more energy-efficient steering control systems that optimize the balance between performance and energy efficiency.

In conclusion, the proposed TD-based 2-DOF dynamic model for skid-steered vehicles effectively addresses the limitations of traditional SD-based models particularly with respect to poor high-frequency response. This model provides a more accurate representation of the vehicle's steering response characteristics, contributing to the advancement of skid-steered vehicle steering dynamics and offering valuable insights for steering control model development.

6. Conclusions

In this study, a linear 2-DOF dynamics model for multi-axle skid-steered wheeled vehicles is discussed. Addressing limitations in SD-based models, a TD-based 2-DOF dynamics model is introduced. With the incorporation of the ICR, steady-state steering radii are computed and the relationship between steering responses and characteristics is analyzed. The steering responses of both SD-based and TD-based models are evaluated through comprehensive real-vehicle testing. It is confirmed that the TD-based model provides superior precision and quicker responses across various steering input frequencies. The key conclusions are outlined as follows:

1. A TD-based linear 2-DOF model is constructed for multi-axle skid-steered wheeled vehicles derived from a single-wheel dynamics model. Stability factors and formulas for characteristic speeds are presented. The stability advantages of US vehicles are sub-

stantiated by the analysis of time-domain and frequency-domain responses. Furthermore, comparing with Ackermann steering reveals that changes in steering methods, without altering vehicle parameters, do not affect the inherent steering characteristics.

2. The steady-state center coordinates are calculated by a TD-based linear 2-DOF dynamics model and the ICR model. It is observed that the ICR of skid-steered vehicles consistently advances as speed increases. Furthermore, variations in the steady-state turning radius under different steering conditions are elucidated: decreasing with increased speed in US vehicles, remaining unchanged in NS vehicles regardless of speed, and decreasing in OS vehicles.
3. The comparative analysis from the real vehicle test validates that the TD-based dynamic model significantly quickens the steering response across varied frequency bands under both step and impulse inputs, also showing enhanced precision. Compared to the high signal-to-noise ratio of SD-based inputs, the TD-based model exhibits a relatively stable response.

Author Contributions: Conceptualization, Y.Z. and S.Y.; methodology, Y.Z., S.Y. and X.L.; theoretical calculation, Y.Z., X.L. and X.G.; validation, S.Y. and X.L.; formal analysis, Y.Z., X.L. and A.L.; experiment, Y.Z., A.L. and X.G.; data processing, Y.Z. and A.L.; writing—original draft preparation, Y.Z., S.Y. and A.L.; writing—review and editing, Y.Z., A.L. and X.G.; supervision, S.Y. and X.L.; project administration, S.Y., X.L. and X.G. All authors have read and agreed to the published version of the manuscript.

Funding: This work was supported by the Fundamental Research Funds for the Central Universities under Grant 2024CX06073.

Data Availability Statement: Data are contained within the article.

Conflicts of Interest: The authors declare no conflicts of interest.

References

1. Zhou, K.; Lei, S.; Du, X. Modelling and dynamic analysis of slippage level for large-scale skid-steered unmanned ground vehicle. *Sci. Rep.* **2022**, *12*, 16014. [CrossRef] [PubMed]
2. Maclaurin, B. Comparing the steering performances of skid- and ackermann-steered vehicles. *Proc. Inst. Mech. Eng. Part D J. Automob. Eng.* **2008**, *222*, 739–756. [CrossRef]
3. Yi, J.; Wang, H.; Zhang, J.; Song, D.; Jayasuriya, S.; Liu, J. Kinematic modeling and analysis of skid-steered mobile robots with applications to low-cost inertial-measurement-unit-based motion estimation. *IEEE Trans. Robot.* **2009**, *25*, 1087–1097.
4. Hu, C.; Wang, R.; Yan, F.; Karimi, H.R. Robust composite nonlinear feedback path-following control for independently actuated autonomous vehicles with differential steering. *IEEE Trans. Transp. Electrif.* **2016**, *2*, 312–321. [CrossRef]
5. Fauroux, J.-C.; Vaslin, P. Modeling, experimenting, and improving skid steering on a 6 × 6 all-terrain mobile platform. *J. Field Robot.* **2010**, *27*, 7–126. [CrossRef]
6. Beal, C.E.; Boyd, C. Coupled lateral-longitudinal vehicle dynamics and control design with three-dimensional state portraits. *Veh. Syst. Dyn.* **2019**, *57*, 286–313. [CrossRef]
7. Zhang, G.; Wang, X.; Li, L.; Zhao, X. Tire–road friction estimation for four-wheel independent steering and driving evs using improved ckf and fnn. *IEEE Trans. Transp. Electrif.* **2024**, *10*, 823–834. [CrossRef]
8. Dogru, S.; Marques, L. A physics-based power model for skid-steered wheeled mobile robots. *IEEE Trans. Robot.* **2018**, *34*, 421–433. [CrossRef]
9. Zhu, Y.; Li, X.; Zhang, X.; Li, S.; Liu, Q.; Yuan, S. Research on tire–road parameters estimation algorithm for skid-steered wheeled unmanned ground vehicle. *Machines* **2022**, *10*, 1015. [CrossRef]
10. Liu, H.; Zhang, L.; Wang, P.; Chen, H. A real-time nmpc strategy for electric vehicle stability improvement combining torque vectoring with rear-wheel steering. *IEEE Trans. Transp. Electrif.* **2022**, *8*, 3825–3835. [CrossRef]
11. Seegmiller, N.; Kelly, A. High-fidelity yet fast dynamic models of wheeled mobile robots. *IEEE Trans. Robot.* **2016**, *32*, 614–625. [CrossRef]
12. Aguilera-Marinovic, S.; Torres-Torriti, M.; Auat-Cheein, F. General dynamic model for skid-steer mobile manipulators with wheel–ground interactions. *IEEE/ASME Trans. Mechatron.* **2016**, *22*, 433–444. [CrossRef]
13. Meldrum, W.R. *Modeling and Simulation of a Differential Torque Steered Wheeled Vehicle*; US Army TARDEC: Warren, MI, USA, 2003.

14. Govindarajan, M.S. Modeling and Simulation of a Six Wheel Differential Torque Steer Vehicle. Master's Thesis, The Pennsylvania State University, University Park, PA, USA, 2010.
15. Ren, F.; Jiang, Z.; Chen, J.; Liu, B. Analysis and experimental research on the characteristic of skid steering vehicle based on a dynamic analysis model. *Multimed. Tools Appl.* **2020**, *79*, 10309–10326. [CrossRef]
16. Ni, J.; Hu, J. Dynamic modelling and experimental validation of a skid-steered vehicle in the pivotal steering condition. *Proc. Inst. Mech. Eng. Part D J. Automob. Eng.* **2017**, *231*, 225–240. [CrossRef]
17. Mortazavizadeh, S.A.; Ghaderi, A.; Ebrahimi, M.; Hajian, M. Recent developments in the vehicle steer-by-wire system. *IEEE Trans. Transp. Electrif.* **2020**, *6*, 1226–1235. [CrossRef]
18. Guo, J.; Gao, H.; Ding, L.; Guo, T.; Deng, Z. Linear normal stress under a wheel in skid for wheeled mobile robots running on sandy terrain. *J. Terramech.* **2017**, *70*, 49–57. [CrossRef]
19. Tang, S.; Yuan, S.; Li, X.; Zhou, J. Dynamic modeling and experimental validation of skid-steered wheeled vehicles with low-pressure pneumatic tires on soft terrain. *Proc. Inst. Mech. Eng. Part D J. Automob. Eng.* **2020**, *234*, 840–856. [CrossRef]
20. Yu, W.; Chuy, O.Y.; Collins, E.G.; Hollis, P. Analysis and experimental verification for dynamic modeling of a skid-steered wheeled vehicle. *IEEE Trans. Robot.* **2010**, *26*, 340–353. [CrossRef]
21. Gupta, N.; Ordonez, C.; Collins, E.G. Dynamically feasible, energy efficient motion planning for skid-steered vehicles. *Auton. Robot.* **2017**, *41*, 453–471. [CrossRef]
22. Narvesen, A.; Selekwa, M.F. Dynamics and control of four wheeled differentially steered ugvs. In *ASME International Mechanical Engineering Congress and Exposition*; American Society of Mechanical Engineers: New York, NY, USA, 2014; Volume 46476, p. V04AT04A034.
23. Zhang, Y.; Hu, J.; Li, X. Steady-state characteristics of skid steering for wheeled vehicles. *Proc. Inst. Mech. Eng. Part D J. Automob. Eng.* **2014**, *228*, 1095–1104. [CrossRef]
24. Zhang, X.; Pei, W.; Yin, X.; Yuan, S. An observation algorithm for key motion states of skid-steered wheeled unmanned vehicle. *Proc. Inst. Mech. Eng. Part D J. Automob. Eng.* **2023**, *237*, 2431–2443. [CrossRef]
25. Ni, J.; Hu, J.; Li, X. Dynamic modelling, validation and handling performance analysis of a skid-steered vehicle. *Proc. Inst. Mech. Eng. Part D J. Automob. Eng.* **2016**, *230*, 514–526. [CrossRef]
26. Mokhiamar, O.; Amine, S. Lateral motion control of skid steering vehicles using full drive-by-wire system. *Alex. Eng. J.* **2017**, *56*, 383–394. [CrossRef]
27. Hu, J.; Zhang, B.; Wang, H.; Zhao, L.; Jiang, P. Coordinated control and torque distribution of differential steering and anti-skid driving of distributed drive electric vehicle considering stability. *Proc. Inst. Mech. Eng. Part D J. Automob. Eng.* **2023**, *237*, 2780–2796.
28. Tan, Y.; Su, X.; Shen, C.; Huang, J. Motion tracking control of six-wheel skid-steering electric vehicles via two-level-sequence-based integrated algorithm. *IEEE Trans. Ind. Electron.* **2024**, *71*, 14937–14945. [CrossRef]
29. Zhang, T. Research on anti-skid-rotation control strategy of dual-motor four-wheel-drive electric vehicle drive. In *Intelligent Transportation and Smart Cities*; IOS Press: Amsterdam, The Netherlands, 2024; pp. 30–45.
30. Kim, T.; Kim, W.; Choi, S.; Kim, H.J. Path tracking for a skid-steer vehicle using model predictive control with on-line sparse gaussian process. *IFAC-PapersOnLine* **2017**, *50*, 5755–5760. [CrossRef]
31. Tarokh, M.; McDermott, G. Kinematics modeling and analyses of articulated rovers. *IEEE Trans. Robot.* **2005**, *21*, 539–553. [CrossRef]
32. Martínez, J.L.; Mandow, A.; Morales, J.; Pedraza, S.; Garcia-Cerezo, A. Approximating kinematics for tracked mobile robots. *Int. J. Robot. Res.* **2005**, *24*, 867–878. [CrossRef]

Disclaimer/Publisher's Note: The statements, opinions and data contained in all publications are solely those of the individual author(s) and contributor(s) and not of MDPI and/or the editor(s). MDPI and/or the editor(s) disclaim responsibility for any injury to people or property resulting from any ideas, methods, instructions or products referred to in the content.